

$\text{Sn}_{0.06}\text{Cr}_3\text{Te}_4$: A Skyrmiон Superconductor

Shubham Purwar^a, Anumita Bose^b, Achintya Low^a, Satyendra Singh^c, R. Venkatesh^c, Awadhesh Narayan^b and Setti Thirupathaiah^a

^aDepartment of Condensed Matter and Materials Physics S. N. Bose National Centre for Basic Sciences Kolkata West Bengal 700106 India.

^bSolid State and Structural Chemistry Unit Indian Institute of Science Bengaluru 560012 India.

^cLow-Temperature Laboratory UGC-DAE Consortium for Scientific Research Indore Madhya Pradesh 452017 India.

ARTICLE INFO

Keywords:

Skyrmion Superconductors
2D Materials
Magnetic Weyl Semimetals
Topological Hall Effect
Skyrmion Lattice

ABSTRACT

Topological superconductors are an exciting class of quantum materials from the point of view of the fundamental sciences and potential technological applications. Here, we report on the successful introduction of superconductivity in a ferromagnetic layered skyrmion system Cr_3Te_4 , obtained by the Sn intercalation, below a transition temperature of $T_c \approx 3.5$ K. We observe several interesting physical properties, such as superconductivity, magnetism, and the topological Hall effect, simultaneously in this system. Despite the magnetism and Meissner effects being anisotropic, the superconductivity observed from the in-plane electrical resistivity (ρ_{bc}) is nearly isotropic between $H \parallel bc$ and $H \parallel a$, suggesting separate channels of conduction electrons responsible for the superconductivity and magnetism of this system, which is also supported by our spin-resolved DFT calculations. We identify two orders of higher carrier density in superconducting $\text{Sn}_{0.06}\text{Cr}_3\text{Te}_4$ than the parent Cr_3Te_4 . A jump in the specific heat is noticed around the T_c with a volume fraction of 33%, confirming the bulk superconductivity in $\text{Sn}_{0.06}\text{Cr}_3\text{Te}_4$. In addition to the introduction of superconductivity, tuning of topological Hall properties is noticed with Sn intercalation. Our observation of superconductivity in a skyrmion lattice brings up a new class of topological quantum materials.

1. Introduction

Superconductivity observed with a topological quantum phase is a much-anticipated phenomenon as it opens a new window of potential technological applications in superconducting electronics, such as topological quantum computations [1]. Thus, designing new materials and their experimental realization is an essential scientific sequence for garnering futuristic quantum technological applications. Several proposals exist for achieving topological superconductivity, such as the hereto-structure of a superconductor and a topological insulator or a doped topological insulator. In topological superconductors, the Cooper pairs are trapped at the vertices of the interface in the form of Majorana fermions due to the proximity effect [2–5] or at the junction of a superconductor and a magnet deposited on the surface of a topological insulator [6]. Nevertheless, several experimental studies were carried out to realize the superconductivity in the presence of quantum topology [7–9].

In addition, superconductivity has been found in many van der Waals (vdW) materials such as NaSn_2As_2 ($T_c = 1.3$ K) [10], $\text{Na}_{1-x}\text{Sn}_2\text{P}_2$ ($T_c = 2$ K) [11], NbSe_2 ($T_c = 6$ K) [12], and $\text{Re}_6\text{Se}_8\text{Cl}_2$ ($T_c = 8$ K) [13]. Further, there exists another class of vdW materials in which the superconductivity is induced by the metal-ion intercalation, such as $\text{A}_x\text{Bi}_2\text{Se}_3$ ($\text{A} = \text{Sr}, \text{Cu}$) [14, 15], $\text{Sn}_{0.5}\text{TaSe}_2$ [16], Sn_xNbSe_2 [17], and Cu_xTiSe_2 [18]. In these systems, the intercalated metal ions act as charge carrier donors, increasing the carrier density near the Fermi level and, thus, the superconductivity.

 awadhesh@iisc.ac.in (A. Narayan); setti@bose.res.in (S. Thirupathaiah)

 www.qmat.in (S. Thirupathaiah)

ORCID(s): 0000-0003-0127-7047 (A. Narayan); 0000-0003-1258-0981 (S. Thirupathaiah)

Most importantly, all these intercalated vdW superconductors are nonmagnetic and do not have chiral spin structure in their pristine phase.

On the other hand, the layered Cr_xTe_y based systems are potential candidates to have chiral spin structures originating the topological skyrmion lattice [19–25]. Notably, these systems are formed by the alternative stacking of Cr-full (CrTe_2 -layer) and Cr-vacant (intercalated Cr-layer) layers along the crystal growth axis [26]. Therefore, the intercalated Cr concentration is critical in forming the magnetic and topological properties. As the van der Waals gap separates CrTe_2 layers, introducing the alien atoms within the vdW gap is quite feasible. We chose to intercalate Sn within the vdW gap of CrTe_2 -layers to induce the superconductivity in a topological ferromagnet, Cr_3Te_4 [22]. This way, the intriguing exotic quantum phases, ferromagnetism, and superconductivity can be achieved in a topological skyrmion lattice. It is worth mentioning here that no study is available to date demonstrating the superconducting phase within a skyrmion lattice. Further, such an experimental observation is quite challenging as the ground state properties like ferromagnetism and superconductivity are found to be competing, if not coexisting, unless the ferromagnetism is weak [27–29].

In this study, we successfully intercalated Sn within the van der Waals gap of topological Cr_3Te_4 to induce superconductivity. We could simultaneously identify all three quantum phases, superconductivity, magnetism, and the topological Hall effect in $\text{Sn}_{0.06}\text{Cr}_3\text{Te}_4$. The pristine Cr_3Te_4 shows a topological Hall resistivity (ρ_{xy}^T) of $240 \text{ n}\Omega - \text{cm}$, but the Sn intercalation significantly reduces it to $16 \text{ n}\Omega - \text{cm}$. In addition, despite the magnetism and Meissner effects being

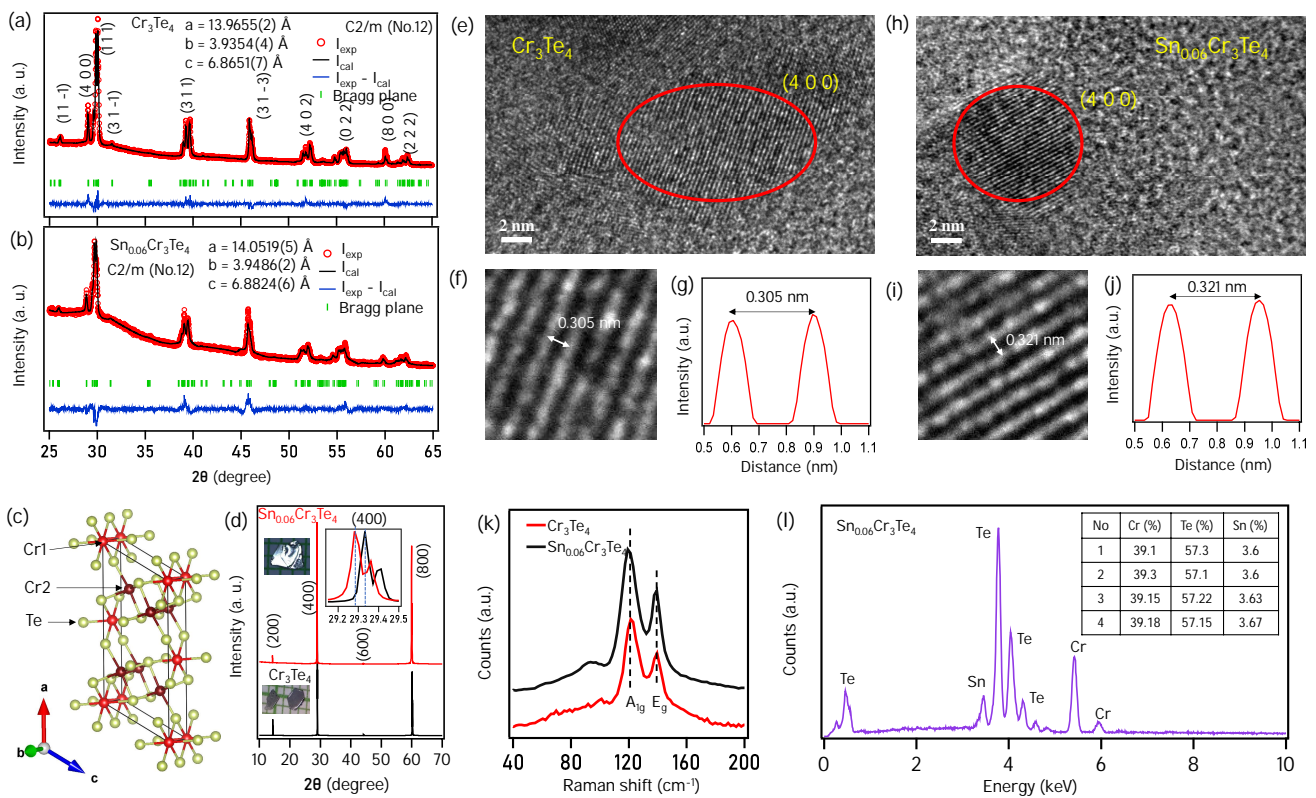


Figure 1: (a) and (b) XRD patterns of the crushed single crystals of Cr_3Te_4 and $\text{Sn}_{0.06}\text{Cr}_3\text{Te}_4$, respectively, overlaid with Rietveld refinement. (c) Schematic image of the monoclinic crystal structure of Cr_3Te_4 . (d) XRD patterns of Cr_3Te_4 (bottom panel) and $\text{Sn}_{0.06}\text{Cr}_3\text{Te}_4$ (top panel) single crystals. Top-middle inset in (c) shows zoomed-in (4 0 0) Bragg's peak demonstrating the lattice shift between the parent and the Sn intercalated samples. Optical images of typical single crystals are shown in the left-side insets of (d). (e) HRTEM image taken on Cr_3Te_4 crystallite, demonstrating the lattice planes corresponding to the (4 0 0) plane. (f) Zoomed-in HRTEM image from (e), displaying the interplanar distance of 0.305 nm. (g) (4 0 0) lattice plane intensity plot confirming the interplanar distance. (h)-(j) Same as (e)-(g) but from $\text{Sn}_{0.06}\text{Cr}_3\text{Te}_4$ crystallite. (k) Raman spectra measured on Cr_3Te_4 and $\text{Sn}_{0.06}\text{Cr}_3\text{Te}_4$ single crystals. (l) EDS spectra measured on four different $\text{Sn}_{0.06}\text{Cr}_3\text{Te}_4$ crystallites, confirming the uniform chemical composition. Atomic weight percentages of respective elements are tabulated in the inset of (l).

anisotropic, the superconductivity observed from the in-plane electrical resistivity (ρ_{bc}) is nearly isotropic between $H \parallel bc$ and $H \parallel a$, suggesting separate channels of conduction electrons responsible for the superconductivity and magnetism of this system, which is supported by our spin-resolved DFT calculations. We identify two orders of higher carrier density in superconducting $\text{Sn}_{0.06}\text{Cr}_3\text{Te}_4$ than the parent Cr_3Te_4 . A jump in the specific heat is noticed around the T_c with a volume fraction of 33%, confirming the bulk superconductivity in $\text{Sn}_{0.06}\text{Cr}_3\text{Te}_4$. Importantly, for the first time, this study demonstrates superconductivity in a skyrmion lattice, offering a new class of topological quantum materials.

2. Methodology

2.1. Experimental Details

Single crystals of Sn intercalated Cr_3Te_4 were grown by the Sn-flux method by mixing high purity elements of Cr (5N, Alfa Aesar) and Te (5N, Alfa Aesar) powders as per the stoichiometric ratio in an alumina crucible, added with Sn (99.998%, Alfa Aesar) shots, and sealed

the crucible inside a quartz ampoule under argon atmosphere. A schematic diagram of the single crystal growth heat treatment is shown in Fig. S1 of the supplemental information. Plate-like single crystals with a typical size of $3 \times 2 \text{ mm}^2$ with a thickness of 0.15 mm were collected after the reaction. Single crystals of Cr_3Te_4 were grown by the chemical vapor transport (CVT) technique with iodine as a transport agent as per the procedure described earlier [30]. Structural and elemental characterizations were performed using an X-ray diffractometer (Rigaku-9kW, Cu K_α of 1.54059 \AA wavelength at Room temperature) and energy dispersive spectroscopy (EDS) techniques, respectively. Temperature-dependent electrical transport, Hall effect, and magnetization measurements were performed using the 9 Tesla physical property measurement system (PPMS, Quantum Design, DynaCool). Electrical resistivity and Hall effect measurements were performed in the standard four-probe method. Temperature-dependent heat capacity measurements were taken using the relaxation method using the Quantum Design-PPMS system. The high-resolution transmission electron microscopy (HRTEM) was done in

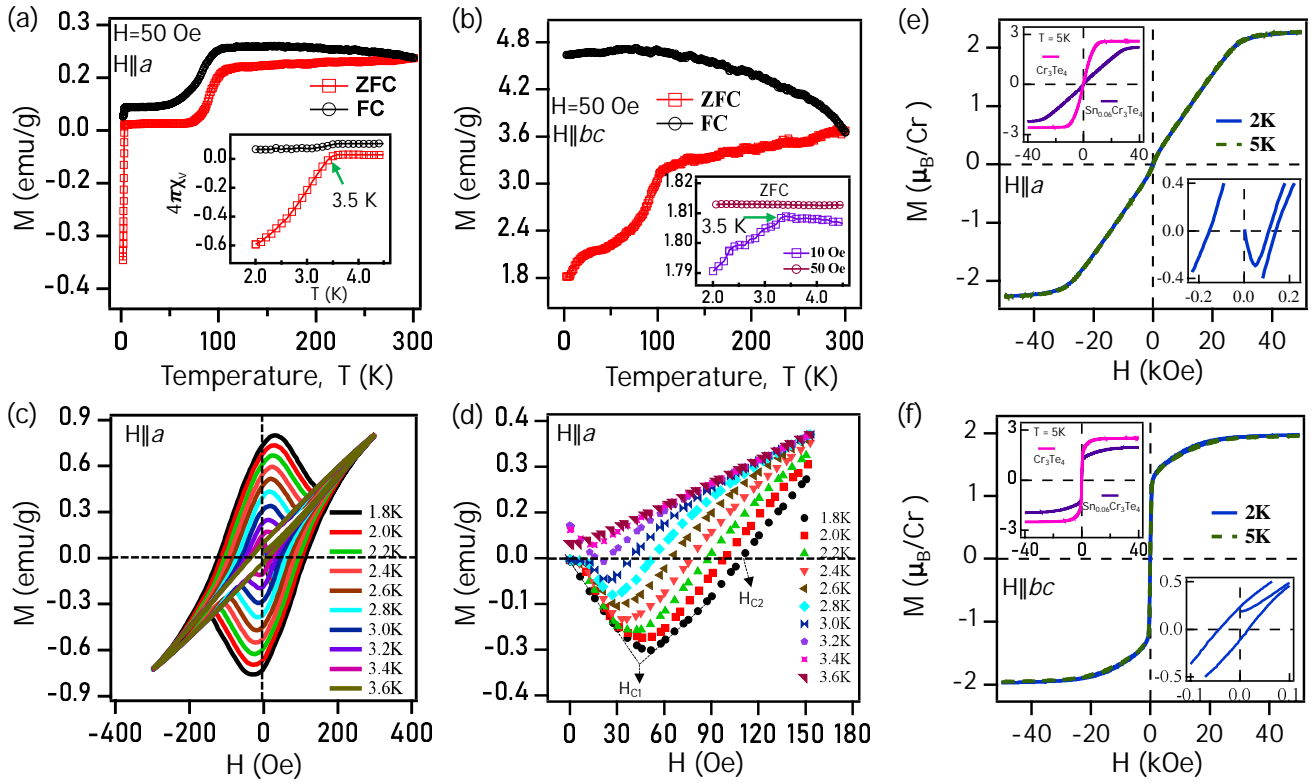


Figure 2: Magnetic properties of Sn_{0.06}Cr₃Te₄ single crystal. (a) Temperature dependent magnetization [M(T)] measured with H = 50 Oe for $H \parallel a$. Inset of (a) shows the susceptibility near the superconducting region. (b) Same as (a) but measured for $H \parallel bc$. Inset of (b) shows overlapped M(T) measured with 10 and 50 Oe. (c) and (d) Show low field Isothermal magnetization [M(H)] curves, demonstrating the Meissner effect within the temperature range of 1.8-3.6 K. H_{c1} and H_{c2} in (d) represent lower and upper critical fields, respectively. (e) M(H) curve measured at 2 and 5 K for $H \parallel a$. Top-left inset in (e) shows M(H) curves measured at 5 K from Cr₃Te₄ and Sn_{0.06}Cr₃Te₄ single crystals for $H \parallel a$. Bottom-right inset of (e) shows zoomed-in M(H), demonstrating the Meissner effect in presence of significant coercive field. (f) M(H) curve measured at 2 and 5 K for $H \parallel bc$. Top-left inset in (f) shows M(H) curves measured at 5 K from Cr₃Te₄ and Sn_{0.06}Cr₃Te₄ single crystals for $H \parallel bc$. Bottom-right inset of (f) shows zoomed-in M(H), demonstrating the absence of Meissner effect for $H \parallel bc$.

an FEI, TECNAI TF 20, S-TWIN microscope operated at 200 KV. The samples were prepared by drop-casting onto a carbon-coated copper grid of a 3 mm diameter. Raman spectra were captured by using a micro-Raman spectrometer (LabRam HR Evolution HORIBA France SAS) equipped with a 532 nm laser.

2.2. DFT Calculations

Spin-polarized DFT calculations have been carried out on Cr₃Te₄ and Sn_{0.06}Cr₃Te₄ (one unit cell consists of 1 Sn, 6 Cr, and 8 Te atoms) based on the projector augmented wave (PAW) method [31] as implemented in the Quantum Espresso package [32, 33]. For the exchange-correlation interaction, we considered the Perdew-Burke-Ernzerhof [34] form of the generalized gradient approximation (GGA). To consider the van der Waals forces, semi-empirical Grimme's DFT-D2 correction [35] was considered. To optimize the atomic positions, a cutoff value of 10⁻³ Ry/Bohr was chosen for the Hellmann-Feynmann forces. A plane wave cutoff of 50 Ry was employed. 4 × 16 × 8 and 8 × 32 × 16 k-mesh with Γ -centered were used for the self-consistency and DOS calculations, respectively.

3. Results and Discussion

Structural Properties:- The exact chemical composition of the Sn intercalated and the parent single crystals was found to be Sn_{0.06}Cr_{2.74}Te₄ and Cr_{2.76}Te₄, respectively, using the EDS measurements. For convenience, we use the nominal composition formula of Cr₃Te₄. Fig. 1(a) shows the XRD pattern of the crushed Cr₃Te₄ single crystals measured at room temperature. All peaks in the XRD pattern can be attributed to the monoclinic crystal structure of the C2/m space group (No.12). This is consistent with the crystal structure of Cr₃Te₄ [36-38]. Rietveld refinement further confirms the monoclinic structure with lattice parameters, $a=13.9655(2)$ Å, $b=3.9354(4)$ Å, $c=6.8651(7)$ Å, $\alpha=\beta=90^\circ$, and $\gamma = 118.326(7)^\circ$ with $\chi^2=2.95$. Similarly, Fig. 1(b) shows the XRD pattern of the crushed Sn_{0.06}Cr₃Te₄ single crystals measured at room temperature. Again, all peaks in the XRD pattern can be attributed to the monoclinic crystal structure of the C2/m space group without any Sn impurity phases. Rietveld refinement further confirms the monoclinic structure with lattice parameters, $a=14.0551(4)$ Å, $b=3.9494(3)$ Å, $c=6.8839(5)$ Å, $\alpha=\beta=90^\circ$, and $\gamma =$

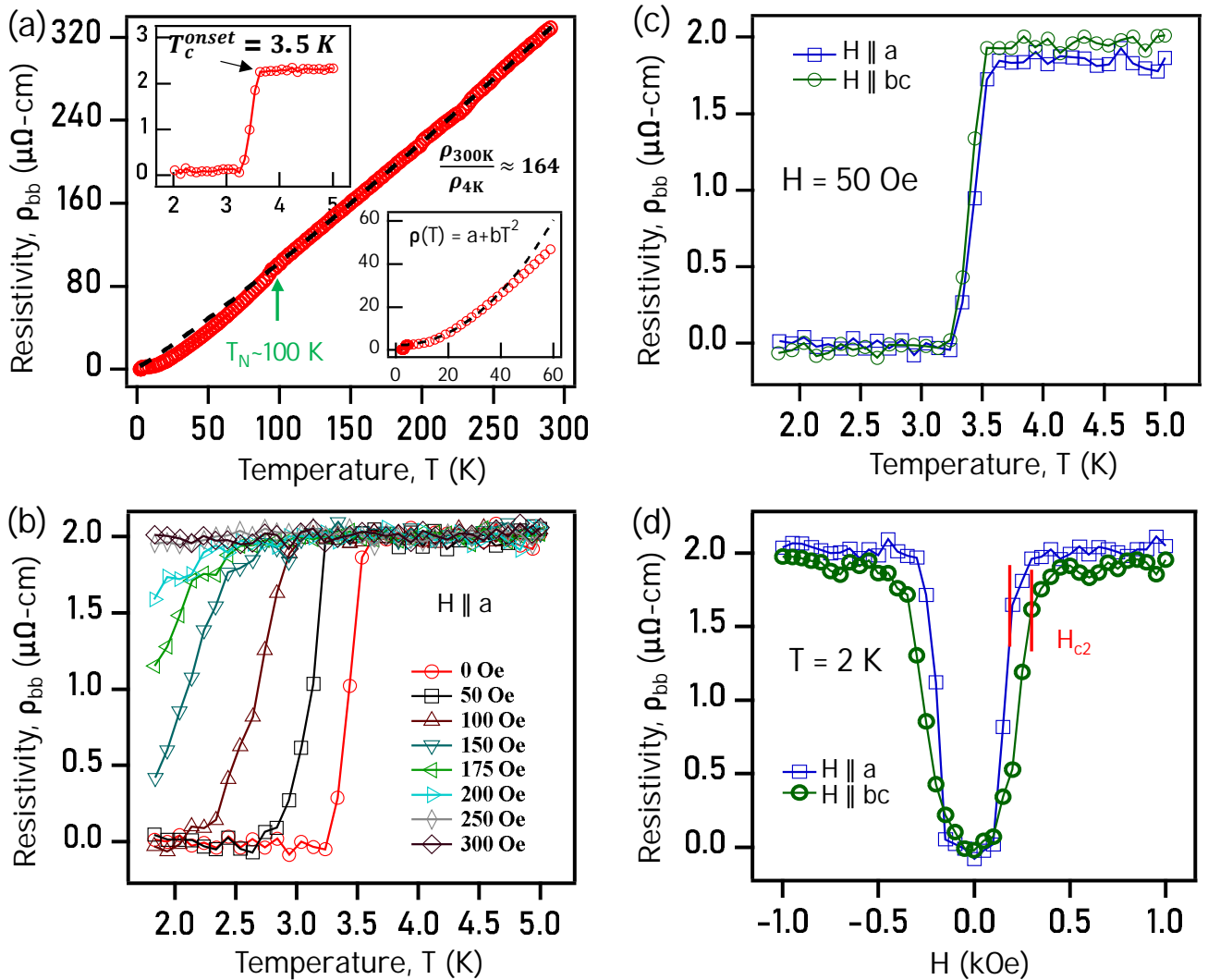


Figure 3: Electrical transport properties of $\text{Sn}_{0.06}\text{Cr}_3\text{Te}_4$ single crystal. (a) Temperature dependent in-plane electrical resistivity ($\rho_{bc}(T)$). Top inset of (a) shows onset superconducting transition of $T_c \approx 3.5$ K. Bottom inset of (a) represents Fermi-liquid fitting at low temperature region. (b) $\rho_{bc}(T)$ measured under various magnetic field within temperature range of 1.8-5 K for $H \parallel a$. (c) $\rho_{bc}(T)$ measured within temperature range of 1.8-5 K for $H \parallel a$ and $H \parallel bc$ at an applied field of 50 Oe. (d) $\rho_{bc}(H)$ measured as a function of field for $H \parallel a$ and $H \parallel bc$ at 2 K.

118.376(7) $^\circ$ with $\chi^2=3.35$. We can see that the Sn intercalation slightly increases the a -axis lattice parameter, while the change in lattice parameters of b and c is negligible. Fig. 1(c) depicts the schematic crystal structure of Cr_3Te_4 in which the alternative staking of Cr(1) and Cr(2) layers is demonstrated along the a -axis.

The XRD patterns taken on the single crystal of Cr_3Te_4 and $\text{Sn}_{0.06}\text{Cr}_3\text{Te}_4$ are shown in the bottom and top panels of Fig. 1(d), respectively, which are consistent with the monoclinic space group of $C2/m$, suggesting that the crystal growth axis is parallel to the a -axis [22, 37, 38]. Inset in Fig 1(d) shows the overlapped (4 0 0) reflections from Cr_3Te_4 and $\text{Sn}_{0.06}\text{Cr}_3\text{Te}_4$ in which the peak position is shifted towards the lower 2θ for $\text{Sn}_{0.06}\text{Cr}_3\text{Te}_4$ compared to Cr_3Te_4 . The XRD peak shifting to a lower 2θ value indicates an expansion of the interplanar spacing along the a -axis due to Sn intercalation [16, 17]. Fig. 1(e) shows the HRTEM

image taken on Cr_3Te_4 crystallite, demonstrating the lattice planes corresponding to the (4 0 0) plane. Fig. 1(f) depicts the zoomed-in HRTEM image of Fig. 1(e), displaying the interplanar distance of 0.305 nm which is in agreement with the interplanar spacing of 0.307 nm [(4 0 0)] derived from the Rietveld refinement. This is further confirmed from the lattice plane intensity plot as shown in Fig. 1(g). Figs. 1(h)-(j) depicts information of (4 0 0) plane as similar as shown in Figs. 1(e)-(g) but from a $\text{Sn}_{0.06}\text{Cr}_3\text{Te}_4$ crystallite. From Figs. 1(i) and 1(j), we can clearly notice that Sn intercalation increases the (4 0 0) interplanar spacing of about 0.016 nm compared to the parent system. This is in good agreement with the XRD peak shifting to lower 2θ angle with Sn intercalation [see inset in Fig. 1(d)].

Next, from the Raman spectra as shown in Fig. 1(k), we mainly observe two prominent phonon peaks, positioned at approximately 123.5 cm^{-1} and 139.79 cm^{-1} . These peaks

correspond to the distinct vibrational modes such as the out-of-plane A_{1g} and the in-plane E_g , of a typical Cr_xTe_y system [39, 40]. This observation confirms that the intercalated Sn atoms take the positions in the Cr(2)-intercalated layer [see Fig. 1(c)]. Importantly, we do not observe any additional Raman modes corresponding to the Sn impurity which shall be at around 202.5 cm^{-1} [41]. Further, to be more accurate on the chemical composition, particularly, of the Sn intercalated system, we performed EDS measurements on several crystallites of $\text{Sn}_{0.06}\text{Cr}_3\text{Te}_4$ as shown Fig. 1(l). From Fig. 1(l), it is evident that the chemical composition is uniform across all the measured crystallites within the error-bars ($\text{Sn}_{0.063(2)}\text{Cr}_{2.74(1)}\text{Te}_4$).

Magnetic Properties:- Magnetization [$M(T)$], plotted as a function of temperature for $\text{Sn}_{0.06}\text{Cr}_3\text{Te}_4$ both field-cooled (FC) and zero-field-cooled (ZFC) modes, measured with a magnetic field of 50 Oe applied parallel to a -axis ($H \parallel a$) is shown in Fig. 2(a) and the field applied parallel to bc -plane ($H \parallel bc$) is shown in Fig. 2(b). The Meissner effect is clearly visible from the ZFC data of $H \parallel a$, as shown in the inset of Fig. 2(a), at an onset transition temperature of 3.5 K, below which the magnetization becomes negative due to diamagnetism in the superconducting phase. In addition to the Meissner effect at 3.5 K, we also identify a sharp decrease in magnetization from FC and ZFC modes at around 100 K, possibly due to a canted antiferromagnetic (AFM) transition [42]. In contrast to $H \parallel a$, the magnetization measured for $H \parallel bc$ shows a different character as demonstrated in Fig. 2(b). Firstly, we do not observe the Meissner effect below 3.5 K from the ZFC data, and secondly, only the ZFC data shows a AFM transition at around 100 K, but not the FC data. In fact, the saturated magnetization derived from the FC data ($M_S \approx 4.65\text{ emu/g}$) at 2 K for $H \parallel bc$ is almost 20 times higher than the saturation magnetization ($M_S \approx 0.23\text{ emu/g}$) of $H \parallel a$, indicating a large magnetic anisotropy present in the system [43]. This, further implies that the bc -plane is the easy magnetization plane with stronger magnetic exchange interactions, suppressing the superconducting state in the bc plane. In support of this, the $M(T)$ data measured with an applied field of 10 Oe for $H \parallel bc$ [see the inset of Fig. 2(b)] shows a slight decrease in magnetization precisely at the onset temperature of 3.5 K, suggesting the coexistence of both magnetism and superconductivity in the bc -plane though the stronger ferromagnetic exchange interactions dominate the Meissner effect.

Isothermal magnetization curves [$M(H)$] across the superconducting transition temperature for $H \parallel a$ are shown in Fig. 2(c). Fig. 2(d) shows the zoomed-in data of Fig. 2(c) taken for positive applied fields. From Fig. 2(d), we notice that at lower fields, the negative magnetization increases linearly with the field up to a lower critical field of H_{c1} . However, beyond a certain field, the negative magnetization starts decreasing with increasing field and approaches zero magnetization at an upper critical field of H_{c2} . This observation is consistent at all measured temperatures up to 3.4 K, indicating $\text{Sn}_{0.06}\text{Cr}_3\text{Te}_4$ to a type-II superconductor [44].

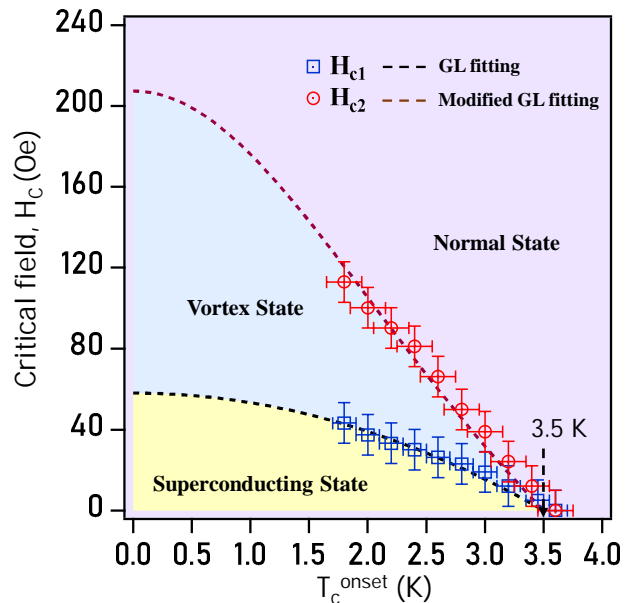


Figure 4: Temperature dependence of lower critical field H_{c1} and upper critical field H_{c2} along with schematic diagram of shaded superconducting, vortex, and normal state regions.

Interestingly, at 3.4 K, despite the magnetization initially decreasing with increasing field like in a typical superconductor, unusually, it is always positive. This could be due to the coexistence of magnetism and superconductivity [45]. Figs. 2(e) and 2(f) show the magnetization isotherms measured at 2 and 5 K for both $H \parallel a$ and $H \parallel bc$, respectively. These data show that the out-of-plane magnetization (a -axis) linearly increases with the field up to 3 T and then saturates to $2.2\text{ }\mu_B/\text{Cr}$. The bottom-right inset of Fig. 2(e) measured at 2 K again demonstrates the superconducting state at lower fields together with a significant coercivity of 150 Oe.

The top-left inset of Fig. 2(e) shows the magnetization isotherms [$M(H)$] measured at 5 K from both parent and the superconducting $\text{Sn}_{0.06}\text{Cr}_3\text{Te}_4$ for $H \parallel a$. From this data, we can see that the magnetization of Cr_3Te_4 saturates faster than that of $\text{Sn}_{0.06}\text{Cr}_3\text{Te}_4$. On the other, the in-plane magnetization (bc -plane) of $\text{Sn}_{0.06}\text{Cr}_3\text{Te}_4$ spontaneously saturates to $2\text{ }\mu_B/\text{Cr}$ under the applied magnetic field as shown in Fig. 2(f), indicating that the bc -plane is the easy-plane of magnetization similar to the parent system [46, 47]. The bottom-right inset of Fig. 2(f) shows the $M(H)$ data measured at 2 K, demonstrating an absence of a superconducting state in the bc -plane even at very low applied fields. The top-left inset of Fig. 2(f) shows magnetization isotherms [$M(H)$] measured at 5 K from both Cr_3Te_4 and the superconducting $\text{Sn}_{0.06}\text{Cr}_3\text{Te}_4$ for $H \parallel bc$. This data shows that the Sn intercalation has no effect on the in-plane magnetization of Cr_3Te_4 except for a slight reduction in the saturated magnetic moment.

Electrical Properties:- In-plane (ρ_{bc}) electrical resistivity of $\text{Sn}_{0.06}\text{Cr}_3\text{Te}_4$ plotted as a function of temperature is shown in Fig. 3(a). At around 100 K, we identify a hump

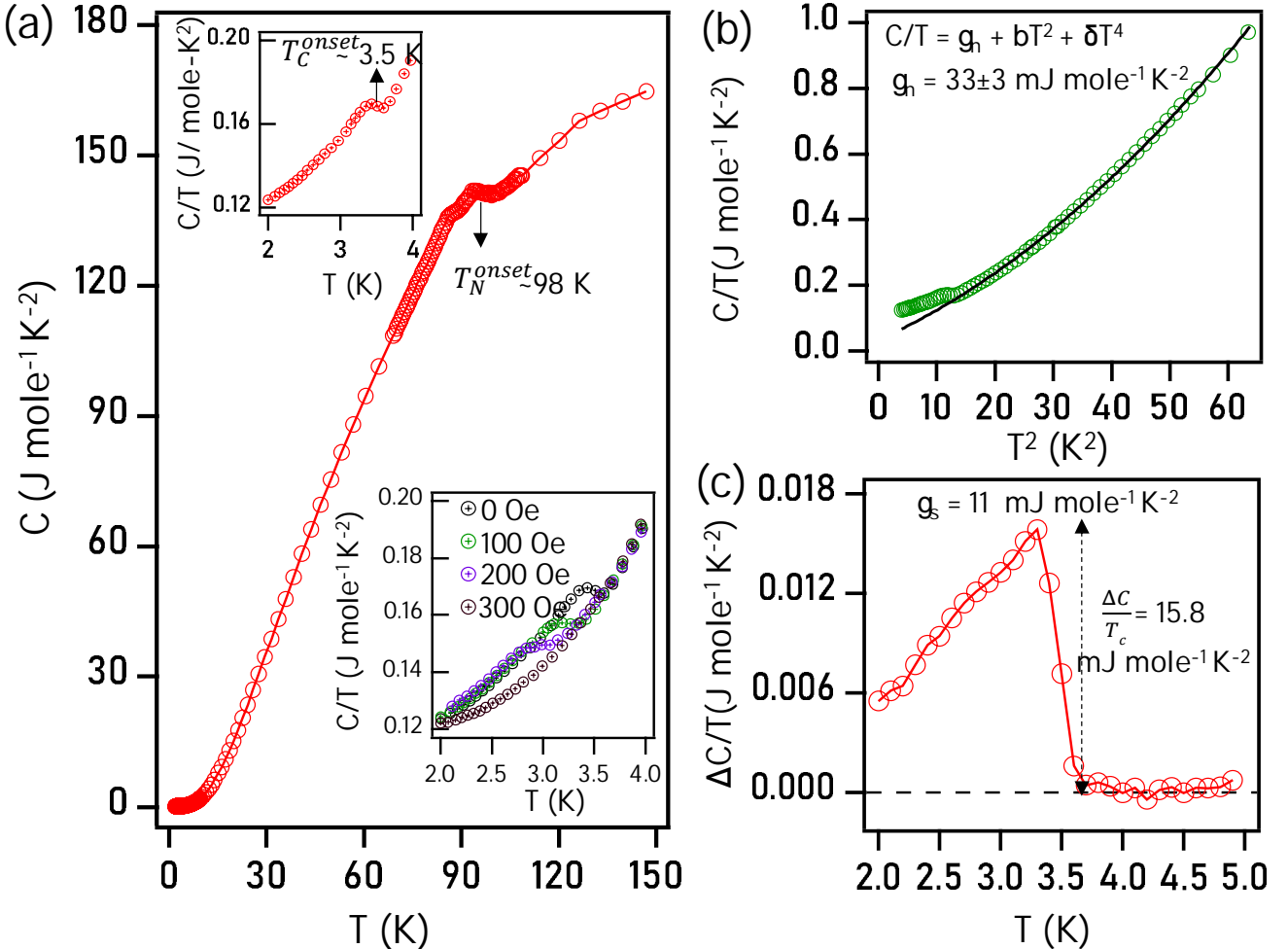


Figure 5: Specific heat $C(T)$ measurements on Sn_{0.06}Cr₃Te₄ single crystal. (a) Temperature dependent $C(T)$. Top-right inset of (a) shows zoomed-in $C(T)$ taken around the T_c . Bottom-left inset of (a) shows $C(T)$ measured under magnetic applied fields. (b) $C(T)$ data fitting using the relation $C(T)/T = \gamma_n + \beta T^2 + \delta T^4$ to extract the Sommerfeld coefficient in the normal state. (c) Depicts $\Delta C/T$ plotted as a function of temperature.

in the resistivity curve due to the AFM transition. The high-temperature resistivity between 100 and 300 K is linearly dependent on the temperature, as the black-dashed-line fitting demonstrates. The top-left inset of Fig. 3(a) demonstrates a drop in resistivity to zero at an onset superconducting transition temperature of $T_c \approx 3.5$ K. The bottom-right inset of Fig. 3(a) suggests Fermi-liquid type electrical resistivity at very low temperatures (< 40 K), as the resistivity quadratically depends on the temperature. In addition, the large residual resistivity ratio (RRR) of $\frac{\rho_{300K}}{\rho_{4K}} \approx 164$ confirms the high quality of the studied samples. Fig. 3(b) shows the electrical resistivity measured by varying the field strength. In Fig. 3(b), a gradual decrease in the onset T_c is noticed with increasing the field. Interestingly, despite the anisotropic magnetization, the superconducting transition temperature is found to be unchanged between $H \parallel a$ and $H \parallel bc$ as $\rho_{bc}(T)$ shows equal onset T_c of 3.5 K when measured with 50 Oe [see Fig. 3(c)]. Fig. 3(d) depicts ρ_{bc} plotted as a function magnetic field for $H \parallel a$ and $H \parallel bc$ at 2 K. We

observe that the upper critical field of $H_{c2} \approx 300$ Oe is higher for $H \parallel bc$ compared to $H_{c2} \approx 200$ Oe for $H \parallel a$.

Critical fields (H_{c1} and H_{c2}) and critical temperatures (T_c) estimated from Fig. 2(d) are plotted in Fig. 4. The data of $H_{c1}(T)$ is reasonably fitted using the Ginzburg-Landau equation of quadratic field dependence on the temperature [48], $H_{c1}(T) = H_{c1}(0)[1 - (T/T_c)^2]$. From the fitting, we obtained a lower critical field of $H_{c1}(0) = 58 \pm 4$ Oe at zero temperature. On the other hand, the upper critical field of $H_{c2}(T)$ is reasonably fitted using the modified Ginzburg-Landau model which takes the form $H_{c2}(T) = H_{c2}(0)[(1 - t^2)/(1 + t^2)]$, where $t = T/T_c$. From this fitting, we obtained an upper critical field of $H_{c2}(0) = 205 \pm 10$ Oe at zero temperature. The Ginzburg-Landau coherence length, $\xi(0) = 1264.8 \pm 90$ Å, is estimated using the relation $H_{c2}(0) = \phi_0/2\pi\xi(0)^2$, where ϕ_0 is the flux quanta. The mean critical field H_c is quantified to 109 ± 9 Oe using the relation, $H_c = \sqrt{H_{c1}H_{c2}}$. Now, by knowing the upper critical field $H_{c2}(0)$ and mean critical field H_c one can estimate the GL parameter (κ) using the relation, $H_{c2}(0) = \sqrt{2}\kappa H_c$. Thus, the obtained

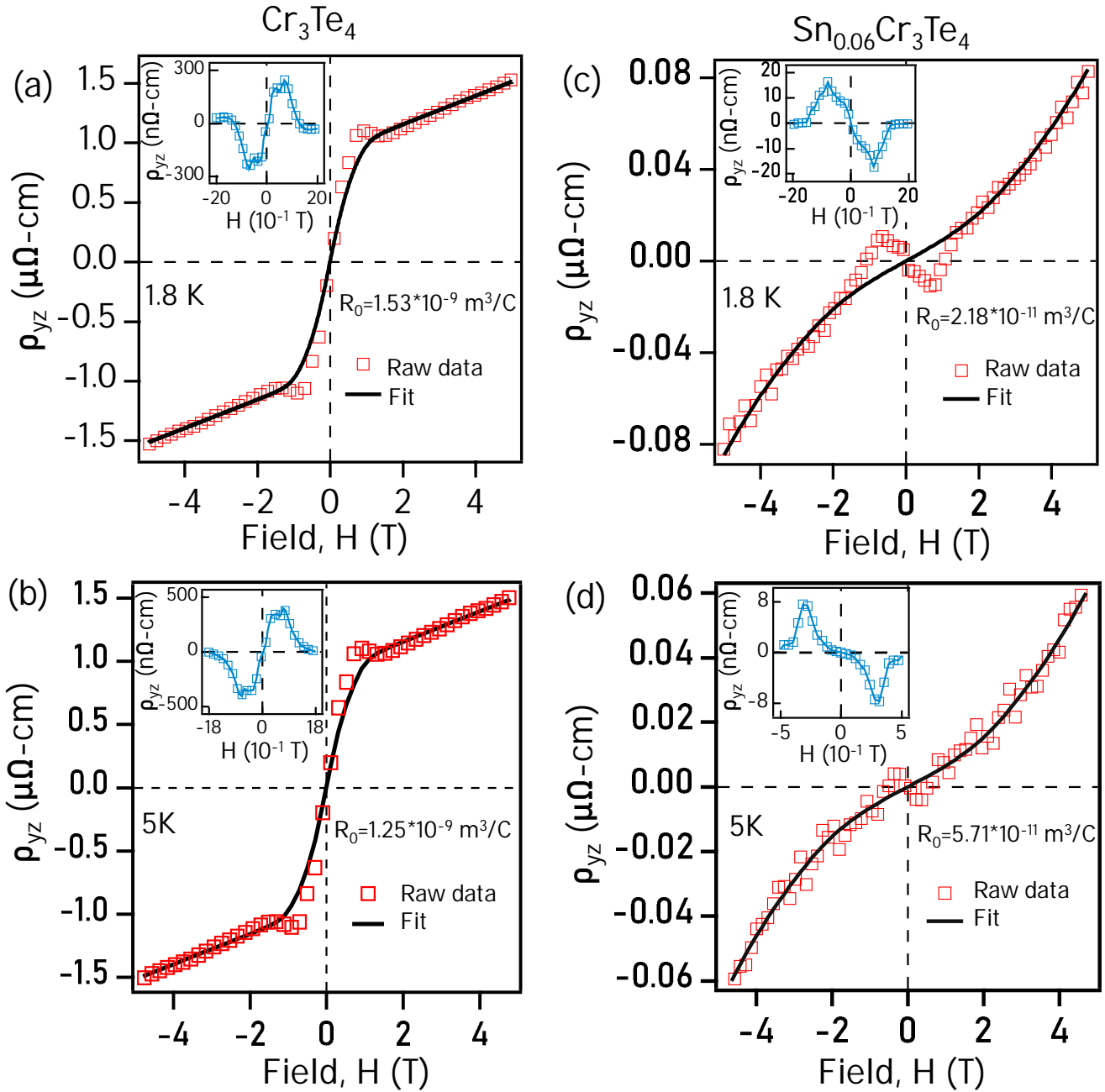


Figure 6: (a) and (b) Hall resistivity (ρ_{xy}) plotted as a function of field for Cr_3Te_4 measured at 1.8 and 5 K, respectively. (c) and (d) are same as (a) and (b) but measured on $\text{Sn}_{0.06}\text{Cr}_3\text{Te}_4$ (b). The black-curves are fits to the data. Insets in (a)-(d) show the topological Hall resistivity plotted as a function of field (see the text for more details).

$\kappa = 1.33$ in this study is well above the threshold value of $\frac{1}{\sqrt{2}}$, again confirming the type-II superconductivity of this system. With the help of GL coherence length ($\xi(0)$) and GL parameter (κ), we further estimated the London penetration depth (λ_L) equal to 1682.1 ± 120 \AA at zero temperature, using the relation $\lambda_L(0) = \kappa \xi(0)$. This value is much larger than any other ferromagnetic superconductor. The mean-free path (l) of the charge carriers is estimated using the relation $l = \hbar k_F / 2\pi \rho_0 n e^2$, where k_F is approximated to $(3\pi^2 n)^{1/3}$ by considering a spherical Fermi surface. Inserting the values,

$\rho_0 = 1.78 \times 10^{-8} \Omega\text{-m}$ and $n = 1.09 \times 10^{29} \text{ m}^{-3}$, we obtained $l = 313.4 \text{ \AA}$. Thus, as $l \ll \xi(0)$, $\text{Sn}_{0.06}\text{Cr}_3\text{Te}_4$ falls in to the dirty-limit of superconductivity [49].

Specific Heat Capacity:- To confirm the bulk superconductivity of $\text{Sn}_{0.06}\text{Cr}_3\text{Te}_4$, we performed specific heat [$C(T)$] measurements within the temperature range of 2-150 K as shown in Fig. 5(a). A specific heat jump at an onset transition temperature $T_c \approx 3.5$ K is noticed from the top-left inset of Fig. 5(a), which is in agreement with the magnetic and transport data shown in Fig. 2(a) and Fig. 3, respectively.

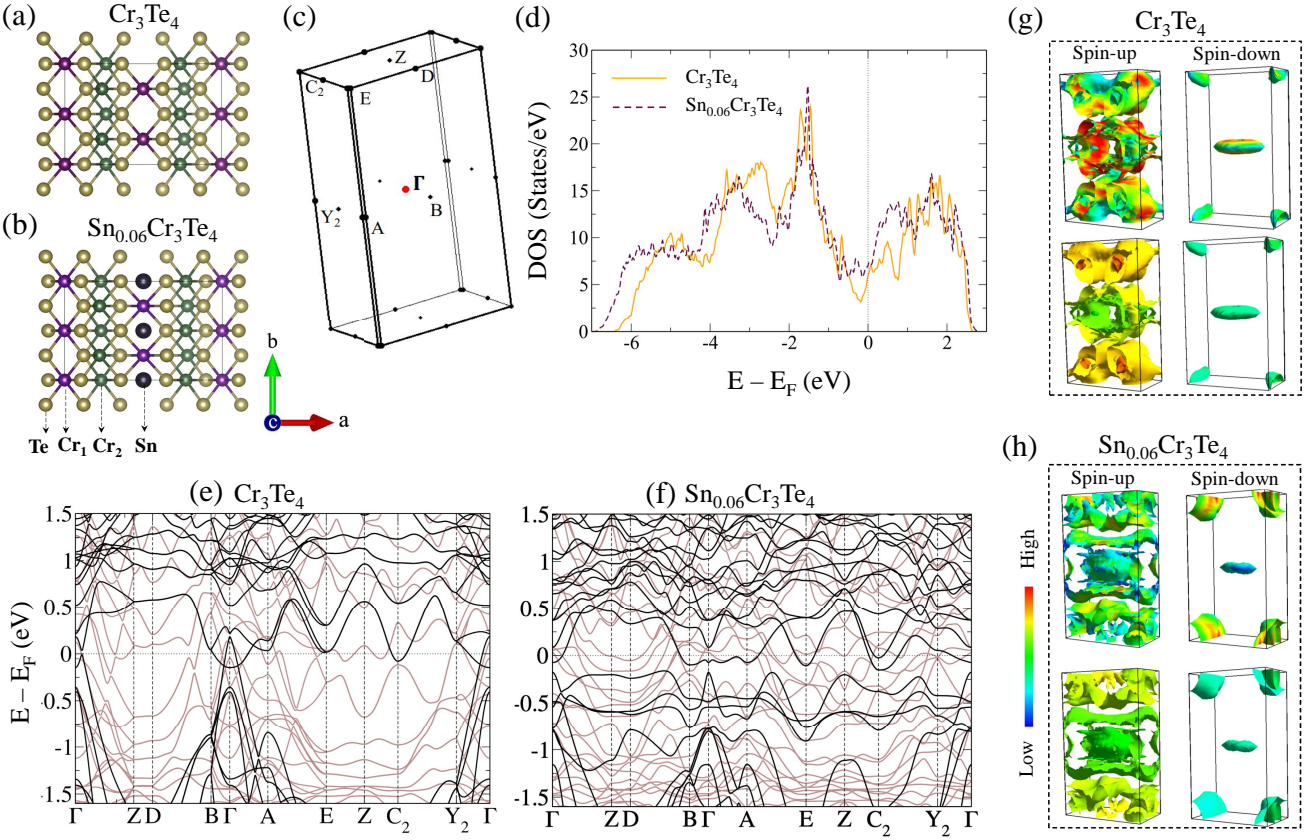


Figure 7: Crystal structure of parent Cr_3Te_4 (a) and $\text{Sn}_{0.06}\text{Cr}_3\text{Te}_4$ (b) projected onto the ab -plane. Magenta, green, yellow and black spheres represent Cr1, Cr2, Te, and Sn atoms, respectively. (c) High symmetry points defined on the monoclinic Brillouin zone. (d) Yellow solid and maroon dashed lines denote the density of states (DOS) for the parent Cr_3Te_4 and $\text{Sn}_{0.06}\text{Cr}_3\text{Te}_4$ systems, respectively. Spin polarised band structures for the parent Cr_3Te_4 (e) and Sn intercalated Cr_3Te_4 (f). Brown and black colours in (e) and (f) denote the bands for the up and down spins, respectively. (g) Fermi surfaces of Cr_3Te_4 plotted for the spin-up and spin-down channels. (h) Fermi surfaces of Sn intercalated Cr_3Te_4 plotted for the spin-up and spin-down channels. The color scale in (g) and (h) represent the Fermi velocity.

The bottom-right inset of Fig. 5(a) depicts the specific heat data measured under various magnetic fields for $H \parallel a$. The T_c and the height of the specific heat jump decrease with increasing the field, and the superconductivity is completely suppressed at an applied field of 300 Oe. In addition, we also observe a specific heat jump around the magnetic transition of 98 K. In Fig. S3(b) of the supplemental information, we provided field-dependent $C(T, H)$ data from which the magnetic transition at 98 K is concluded to be an AFM-type. From Fig. 5(a), we observe the Debye-type increase in heat capacity with temperature up to 150 K, and beyond 150 K it reaches the Dulong-Petit limit. In agreement to this observation, the calculated heat capacity $C = 176.1 \text{ J mole}^{-1} \text{ K}^{-1}$, following the Dulong-Petit law [$C = 3nR$], is close to the experimental heat capacity value at 150 K ($C = 165 \text{ J mole}^{-1} \text{ K}^{-1}$). Here $n = 7.06$ is the number of atoms per formula unit ($\text{Sn}_{0.06}\text{Cr}_3\text{Te}_4$) and $R = 8.3144598 \text{ J mole}^{-1} \text{ K}^{-1}$ is the universal gas constant.

Further, we could reasonably fit the normal state heat capacity data, taken at zero fields, following the relation $C(T) = \gamma_n T + \beta T^3 + \delta T^5$ [see Fig. 5(b)]. Here, the first term ($\gamma_n T$) represents the electronic contribution, and the

second and third terms ($\beta T^3 + \delta T^5$) represent the phonon contribution to the total heat capacity. From the fitting, we derived a Sommerfeld coefficient (γ_n) of the electronic specific heat in the normal state $\gamma_n = 33 \pm 3 \text{ mJ mole}^{-1} \text{ K}^{-2}$ and the coefficients related to the phonon contribution (Debye constants) $\beta = 8 \pm 0.2 \text{ mJ mole}^{-1} \text{ K}^{-4}$ and $\delta = 0.1 \pm 0.04 \text{ mJ mole}^{-1} \text{ K}^{-6}$. We also estimated the Sommerfeld coefficient in the superconducting state $\gamma_s = 11 \text{ mJ mole}^{-1} \text{ K}^{-2}$ [see Fig. 5(c)] using the BCS equation of the weak-coupling limit, $\Delta C/T_c = [C(H = 0 \text{ Oe}) - C(H = 300 \text{ Oe})]/T_c = 1.43 * \gamma_s$. Finally, the superconducting volume fraction is estimated using the relation $\frac{\gamma_s}{\gamma_n} \times 100 \approx 33 \pm 4\%$ [50], which is much larger than the Sn concentration (8%) present in $\text{Sn}_{0.06}\text{Cr}_3\text{Te}_4$. Thus, the large SC volume fraction rules out the Sn impurity phase superconductivity.

Topological Hall Effect: The parent Cr_3Te_4 is known to show significant topological Hall effect (THE) originated by the skyrmion lattice [22, 51, 52]. In order to uncover the presence of THE in the superconducting $\text{Sn}_{0.06}\text{Cr}_3\text{Te}_4$, we performed Hall measurements on both Cr_3Te_4 and $\text{Sn}_{0.06}\text{Cr}_3\text{Te}_4$ as shown in Fig. 6. Figs. 6(a) and 6(b) show

the field dependent total Hall resistivity $\rho_{yz}(H)$ of Cr₃Te₄ measured at 1.8 K and 5 K, respectively. Similarly, Figs. 6(c) and 6(d) show $\rho_{yz}(H)$ of Sn_{0.06}Cr₃Te₄ measured at 1.8 K and 5 K, respectively. ρ_{yz} is measured with current along the y -axis and magnetic field applied along the x -axis to get the Hall voltage along the z -axis. The total Hall resistivity (ρ_{yz}) may have contributions from the normal Hall effect (ρ^N) and the anomalous Hall effect (ρ^A). Thus, the total Hall resistivity can be expressed by the empirical formula, $\rho_{yz}(H) = \rho^N(H) + \rho^A(H) = \mu_0 R_0 H + \mu_0 R_S M$, where R_0 and R_S are the normal and anomalous Hall coefficients, respectively. The fitting (black curves) should be nearly perfect if there is no topological Hall contribution. However, from Figs. 6 (a)-(d), we can notice that the fitting is not perfect. Therefore, the topological Hall resistivity also contributes to the total Hall resistivity, which is expressed by $\rho_{yz}(H) = \rho^N(H) + \rho^A(H) + \rho^T(H)$. Thus, the topological Hall contribution is extracted using the relation, $\rho^T(H) = \rho_{yz}(H) - [\rho^N(H) + \rho^A(H)]$ [53–55] which are shown in the insets of Figs. 6 (a)-(d).

Further, as can be seen from the insets of Figs. 6 (a) and (b), at 2 K, a maximum topological Hall resistivity of $\rho_{xy}^T \approx 240 \text{ n}\Omega - \text{cm}$ is found in Cr₃Te₄ at a critical field of 0.7 T, while $\rho_{xy}^T \approx 16 \text{ n}\Omega - \text{cm}$ is observed from Sn_{0.06}Cr₃Te₄ around at the same critical field of 0.8 T. On the other hand, at 5 K, the maximum topological Hall resistivity of $8 \text{ n}\Omega - \text{cm}$ is observed in Sn_{0.06}Cr₃Te₄ at a critical field of 0.3 T whereas in Cr₃Te₄ we observe a slight increase in ρ_{xy}^T to $345 \text{ n}\Omega - \text{cm}$. An inverted topological Hall signal between Cr₃Te₄ and Sn_{0.06}Cr₃Te₄ [see the insets of Figs. 6(a) and 6(c)] hints at the helicity switching of the skyrmion lattice [56, 57]. These observations demonstrates a tuning of topological properties in Cr₃Te₄ by the Sn intercalation. Importantly, we successfully demonstrate the topological Hall effect in the presence of superconducting state, implying the coexistence of exotic quantum phases skyrmion lattice and superconductivity. Next, the carrier concentration (n) of Cr₃Te₄ and Sn_{0.06}Cr₃Te₄ is calculated by using the formula $n = 1/(R_0|q|)$, where q is the carrier charge. We obtained the carrier concentration (n) of $4.07 \times 10^{21} \text{ cm}^{-3}$ and $2.86 \times 10^{23} \text{ cm}^{-3}$ from Cr₃Te₄ and Sn_{0.06}Cr₃Te₄ at 2 K, respectively. On the other hand, at 5 K, these values are given by $5.01 \times 10^{21} \text{ cm}^{-3}$ and $1.10 \times 10^{23} \text{ cm}^{-3}$ from Cr₃Te₄ and Sn_{0.06}Cr₃Te₄, respectively. This clearly indicates that the Sn intercalation enhances the carrier density in Cr₃Te₄ by an order of two. The hole carrier density of Cr₃Te₄ estimated in this study is consistent with previous reports [58, 59].

Several mechanisms are proposed to understand the topological Hall effect in quantum materials. Such as the Dzyaloshinskii–Moriya (DM) interaction in the noncentrosymmetric systems [60–62] or the uniaxial magnetocrystalline anisotropy (MCA) in the centrosymmetric systems [63–66]. In our present case of the centrosymmetric Cr₃Te₄, the chiral-spin structure is stabilized by the strong MCA as already reported earlier by the same authors [22]. The chiral-spin structure is crucial to obtain the THE as the itinerant electrons acquire a real-space Berry curvature associated

with finite scalar-spin chirality $\chi_{ijk} = S_i \cdot (S_j \times S_k)$ which serves as fictitious magnetic field to generate the topological Hall signal [67–69]. An array of chiral-spin structures can form a lattice structure called the skyrmion lattice. Our findings of topological Hall effect in Cr₃Te₄ and Sn_{0.06}Cr₃Te₄ are consistent with earlier studies on Cr_xTe_y-type systems demonstrating the presence of skyrmion lattice [19, 20, 25, 70].

Electronic Band Structure:- Our experimental results of increased charge carrier density with Sn intercalation are qualitatively supported by the density functional theory (DFT) calculations. For the DFT calculations, we considered the conventional unit cell of Cr₃Te₄, consisting of 6 Cr atoms (2 Cr1-type and 4 Cr2-type) and 8 Te atoms per unit cell as shown in Fig. 7(a). For the Sn intercalated Cr₃Te₄, we considered one Sn atom per primitive unit cell [see Fig. 7(b)]. From the DFT calculations, we find that Cr₃Te₄ is a ferromagnetic metal with an average magnetic moment of $3.32 \mu_B/\text{Cr}$. With the intercalation of Sn, the metallicity and ferromagnetic nature persist, but the average magnetic moment slightly reduces to $3.29 \mu_B/\text{Cr}$. These values are slightly higher than the experimental values of $2.56 \mu_B/\text{Cr}$ for Cr₃Te₄ [36, 71] and $2.10 \mu_B/\text{Cr}$ for Sn_{0.06}Cr₃Te₄ when measured at 2 K. Fig. 7(d) shows the total density of states (DOS) plotted for Cr₃Te₄ and 8% Sn intercalated Cr₃Te₄. We observe that the density of states (DOS) of Sn_{0.06}Cr₃Te₄, near the Fermi level, are significantly increased compared to the DOS of Cr₃Te₄. This behaviour is consistent with the experimental observation of enhanced charge carrier density with Sn intercalation. Moreover, the calculated Fermi energy of $E_F = 9.4650 \text{ eV}$ for Cr₃Te₄ increases to 10.9425 eV by the Sn intercalation. That means, the Fermi energy is shifted by about 1.5 eV towards the higher kinetic energy due to a significant change in the low-energy electronic structure of Cr₃Te₄ with the Sn intercalation. We also performed DFT+U calculations [72] for different values of U ranging up to $U = 3 \text{ eV}$ [see Fig. S4 in the supplemental information]. Interestingly, for all the values of U up to 1 eV, the calculations show enhanced DOS near the Fermi energy in Sn_{0.06}Cr₃Te₄ compared to Cr₃Te₄ [see Fig. S5 in the supplemental information]. However, for $U = 2 \text{ eV}$ and higher we do not find a significant difference in the DOS near E_F between Sn_{0.06}Cr₃Te₄ and Cr₃Te₄.

From the spin-resolved PDOS (see Fig. S5 of the supplemental information), we identify that the Cr 3d orbitals dominate the spin-up DOS near the Fermi level, while they have a negligible contribution to the spin-down DOS. Specifically, we notice that the spin-up DOS is dominated by d_{xy} , $d_{x^2-y^2}$, and d_{zx} orbitals in the vicinity of Fermi level. However, by the Sn intercalation, we notice a decrease in the spin-up DOS and drastic increase (about two times) in the spin-down DOS of $d_{x^2-y^2}$ and d_{zx} . On the other hand, the change in d_{xy} DOS is almost negligible by the Sn intercalation. This clearly indicates that the orbitals, $d_{x^2-y^2}$ and d_{zx} are critical for the superconductivity in Sn_{0.06}Cr₃Te₄. Having understood the orbital contribution near the Fermi level, we then went on to examine the band dispersions [see Figs. 7(e) and 7(f)] and

Fermi surfaces [see Figs. 7(g) and 7(h)]. It is evident from the band dispersions that the Sn intercalation not only shifts the Fermi level to higher kinetic energies but significantly alters the band structure near the Fermi level. Particularly, from a closer look at the spin-down Fermi surface of Cr₃Te₄, we notice an almost equal size of the hole ($k_F = 0.12$ au) and electron ($k_F = 0.16$ au) pockets at the Brillouin zone center and zone corner, respectively [see Fig. 7(g)]. This observation hints at a possibility of Fermi surface nesting as observed from the unconventional superconductors such as in the Fe-based [73–75] and Cu-based [76, 77] systems in their magnetic state. Moreover, by the Sn intercalation, the size of the electron pocket increases at the zone corner, while the hole pockets are barely visible at the zone center [see Fig. 7(h)]. Thus, the reduced Fermi surface nesting is demonstrated in the superconducting state of Sn_{0.06}Cr₃Te₄, again consistent with BaFe_{2-x}Co_xAs₂ superconductor in which the highest T_c was obtained when the size of the hole pockets at the zone center is significantly reduced [78].

4. Conclusions

In conclusion, we successfully induced superconductivity in the topological vdWs ferromagnetic Cr₃Te₄ by Sn intercalation at an onset transition temperature of $T_c \approx 3.5$ K. We conclude that Sn_{0.06}Cr₃Te₄ is a type-II superconductor with a lower critical field of $H_{c1} = 58 \pm 4$ Oe and an upper critical field of $H_{c2} = 209 \pm 10$ Oe. A jump in the specific heat noticed around the T_c with a volume fraction of 33% confirms the bulk superconductivity in Sn_{0.06}Cr₃Te₄. Spin-polarized DFT calculations on Cr₃Te₄ and Sn_{0.06}Cr₃Te₄ provide a better understanding on the orbital contributions near the Fermi level. Tuning of topological Hall effect originating from the skyrmiон lattice is noticed with Sn intercalation in Cr₃Te₄. Most importantly, for the first time, this study demonstrates superconductivity in a skyrmiон lattice, offering a new class of topological quantum materials.

5. Acknowledgments

A.B. acknowledges support from the Prime Minister's Research Fellowship (PMRF). S.G. acknowledges University Grants Commission (UGC), India for the Ph.D. fellowship. A.N. thanks the startup grant of the Indian Institute of Science (SG/MHRD-19-0001) and DST-SERB (SRG/2020/000153). S.T. thanks the Science and Engineering Research Board (SERB), Department of Science and Technology (DST), India, for the financial support (Grant No.SRG/2020/000393).

6. Data availability

The raw and processed data required to reproduce these findings will be made available upon request to the corresponding authors.

References

- [1] C. Nayak, S. H. Simon, A. Stern, M. Freedman, S. Das Sarma, Non-Abelian anyons and topological quantum computation, *Rev. Mod. Phys.* 80 (2008) 1083–1159.
- [2] L. Fu, C. L. Kane, Superconducting Proximity Effect and Majorana Fermions at the Surface of a Topological Insulator, *Phys. Rev. Lett.* 100 (2008) 096407.
- [3] J. Nilsson, A. R. Akhmerov, C. W. J. Beenakker, Splitting of a Cooper Pair by a Pair of Majorana Bound States, *Phys. Rev. Lett.* 101 (2008) 120403.
- [4] M. Veldhorst, M. Snelder, M. Hoek, T. Gang, V. K. Guduru, X. L. Wang, U. Zeitler, W. G. van der Wiel, A. A. Golubov, H. Hilgenkamp, A. Brinkman, Josephson supercurrent through a topological insulator surface state, *Nat. Mater.* 11 (2012) 417–421.
- [5] H. D. Scammell, J. Ingham, M. Geier, T. Li, Intrinsic first- and higher-order topological superconductivity in a doped topological insulator, *Phys. Rev. B* 105 (2022) 195149.
- [6] L. Fu, C. L. Kane, Probing Neutral Majorana Fermion Edge Modes with Charge Transport, *Phys. Rev. Lett.* 102 (2009) 216403.
- [7] A. R. Akhmerov, J. Nilsson, C. W. J. Beenakker, Electrically Detected Interferometry of Majorana Fermions in a Topological Insulator, *Phys. Rev. Lett.* 102 (2009) 216404.
- [8] L. A. Wray, S.-Y. Xu, Y. Xia, Y. S. Hor, D. Qian, A. V. Fedorov, H. Lin, A. Bansil, R. J. Cava, M. Z. Hasan, Observation of topological order in a superconducting doped topological insulator, *Nat. Phys.* 6 (2010) 855–859.
- [9] A. Banerjee, A. Sundaresh, R. Ganesan, P. S. A. Kumar, Signatures of Topological Superconductivity in Bulk-Insulating Topological Insulator Bi₂Sb_{1.25}Se_{1.75} in Proximity with Superconducting NbSe₂, *ACS Nano* 12 (2018) 12665–12672.
- [10] Y. Goto, A. Yamada, T. D. Matsuda, Y. Aoki, Y. Mizuguchi, SnAs-based layered superconductor NaSn₂As₂, *J. Phys. Soc. Japan* 86 (2017) 123701.
- [11] Y. Goto, A. Miura, C. Moriyoshi, Y. Kuroiwa, T. D. Matsuda, Y. Aoki, Y. Mizuguchi, $Na_{1-x}Sn_2P_2$ as a new member of van der Waals-type layered pnictide superconductors, *Sci. Rep.* 8 (2018) 1–8.
- [12] X. Xiaoxiang, et al., Strongly enhanced cdws in monolayer nbse₂, *Nature nanotechnology* 10 (2015) 765–769.
- [13] E. J. Telford, J. C. Russell, J. R. Swann, B. Fowler, X. Wang, K. Lee, A. Zangiabadi, K. Watanabe, T. Taniguchi, C. Nuckolls, et al., Doping-induced superconductivity in the van der Waals superatomic crystal $Re_6Se_8Cl_2$, *Nano Lett.* 20 (2020) 1718–1724.
- [14] Shruti, V. K. Maurya, P. Neha, P. Srivastava, S. Patnaik, Superconductivity by Sr intercalation in the layered topological insulator Bi₂Se₃, *Phys. Rev. B* 92 (2015) 020506.
- [15] Y. S. Hor, A. J. Williams, J. G. Checkelsky, P. Roushan, J. Seo, Q. Xu, H. W. Zandbergen, A. Yazdani, N. P. Ong, R. J. Cava, Superconductivity in Cu_xBi₂Se₃ and its Implications for Pairing in the Undoped Topological Insulator, *Phys. Rev. Lett.* 104 (2010) 057001.
- [16] M. L. Adam, Z. Liu, O. A. Moses, X. Wu, L. Song, Superconducting properties and topological nodal lines features in centrosymmetric Sn_{0.5}TaSe₂, *Nano Res.* 14 (2021) 2613–2619.
- [17] S. Naik, G. K. Pradhan, S. G. Bhat, B. C. Behera, P. A. Kumar, S. L. Samal, D. Samal, The effect of Sn intercalation on the superconducting properties of 2H – NbSe₂, *Phys. C Supercond. Its Appl.* 561 (2019) 18–23.
- [18] E. Morosan, H. W. Zandbergen, B. S. Dennis, J. W. G. Bos, Y. Onose, T. Klimeczuk, A. P. Ramirez, N. P. Ong, R. J. Cava, Superconductivity in Cu_xTiSe₂, *Nature Physics* 2 (2006) 544–550.
- [19] J. Liu, B. Ding, J. Liang, X. Li, Y. Yao, W. Wang, Magnetic Skyrmiон Bubbles at Room Temperature and Sign Reversal of the Topological Hall Effect in a Layered Ferromagnet Cr_{0.87}Te, *ACS Nano* 16 (2022) 13911.
- [20] R. Saha, H. L. Meyerheim, B. Göbel, B. K. Hazra, H. Deniz, K. Mohseni, V. Antonov, A. Ernst, D. Knyazev, A. Bedoya-Pinto, I. Mertig, S. S. P. Parkin, Observation of Neel-type skyrmiонs in acentric self-intercalated Cr_{1+x}Te₂, *Nat. Commun.* 13 (2022).

[21] B. Li, X. Deng, W. Shu, X. Cheng, Q. Qian, Z. Wan, B. Zhao, X. Shen, R. Wu, S. Shi, H. Zhang, Z. Zhang, X. Yang, J. Zhang, M. Zhong, Q. Xia, J. Li, Y. Liu, L. Liao, Y. Ye, L. Dai, Y. Peng, B. Li, X. Duan, Air-stable ultrathin Cr₃Te₄ nanosheets with thickness-dependent magnetic skyrmions, *Materials Today* 57 (2022) 66–74.

[22] S. Purwar, A. Low, A. Bose, A. Narayan, S. Thirupathaiah, Investigation of the anomalous and topological Hall effects in layered monoclinic ferromagnet Cr_{2.76}Te₄, *Phys. Rev. Mater.* 7 (2023) 094204.

[23] Y. Fujisawa, M. Pardo-Almanza, C.-H. Hsu, A. Mohamed, K. Yamagami, A. Krishnadas, G. Chang, F.-C. Chuang, K. H. Khoo, J. Zang, A. Soumyanarayanan, Y. Okada, Widely Tunable Berry Curvature in the Magnetic Semimetal Cr_{1+δ}Te₂, *Adv. Mater.* 35 (2023) 2207121.

[24] H. Chi, Y. Ou, T. B. Eldred, W. Gao, S. Kwon, J. Murray, M. Dreyer, R. E. Butera, A. C. Foucher, H. Ambaye, J. Keum, A. T. Greenberg, Y. Liu, M. R. Neupane, G. J. de Coster, O. A. Vail, P. J. Taylor, P. A. Folkes, C. Rong, G. Yin, R. K. Lake, F. M. Ross, V. Lauter, D. Heiman, J. S. Moodera, Strain-tunable Berry curvature in quasi-two-dimensional chromium telluride, *Nat. Commun.* 14 (2023).

[25] C. Zhang, C. Liu, J. Zhang, Y. Yuan, Y. Wen, Y. Li, D. Zheng, Q. Zhang, Z. Hou, G. Yin, K. Liu, Y. Peng, X.-X. Zhang, Room-Temperature Magnetic Skyrmions and Large Topological Hall Effect in Chromium Telluride Engineered by Self-Intercalation, *Adv. Mater.* 35 (2023) 2205967.

[26] J. Dijkstra, H. H. Weitering, C. F. van Bruggen, C. Haas, R. A. de Groot, Band-structure calculations, and magnetic and transport properties of ferromagnetic chromium tellurides (CrTe, Cr₃Te₄, Cr₂Te₃), *J. Phys.: Condens. Matter* 1 (1989) 9141–9161.

[27] C. Pfleiderer, M. Uhlarz, S. M. Hayden, R. Vollmer, H. v. Löhneysen, N. R. Bernhoeft, G. G. Lonzarich, Coexistence of superconductivity and ferromagnetism in the d-band metal ZrZn₂, *Nature* 412 (2001) 58–61.

[28] C. Y. Yang, B. C. Chang, H. C. Ku, Y. Y. Hsu, Critical fields and the spontaneous vortex state in the weakly ferromagnetic superconductor RuSr₂GdCu₂O₈, *Phys. Rev. B* 72 (2005) 174508.

[29] N. T. Huy, A. Gasparini, D. E. de Nijs, Y. Huang, J. C. P. Klaasse, T. Gortenmulder, A. de Visser, A. Hamann, T. Görlich, H. v. Löhneysen, Superconductivity on the Border of Weak Itinerant Ferromagnetism in UCoGe, *Phys. Rev. Lett.* 99 (2007) 067006.

[30] T. Hashimoto, K. Hoya, M. Yamaguchi, I. Ichitsubo, Magnetic Properties of Single Crystals Cr₂Te₃, *J. Phys. Soc. Japan* 31 (1971) 679–682.

[31] P. E. Blöchl, Projector augmented-wave method, *Phys. Rev. B* 50 (1994) 17953–17979.

[32] P. Giannozzi, S. Baroni, N. Bonini, M. Calandra, R. Car, C. Cavazzoni, D. Ceresoli, G. L. Chiarotti, M. Cococcioni, I. Dabo, et al., QUANTUM ESPRESSO: a modular and open-source software project for quantum simulations of materials, *J. Phys. Condens. Matter* 21 (2009) 395502.

[33] P. Giannozzi, O. Andreussi, T. Brumme, O. Bunau, M. B. Nardelli, M. Calandra, R. Car, C. Cavazzoni, D. Ceresoli, M. Cococcioni, et al., Advanced capabilities for materials modelling with Quantum ESPRESSO, *J. Phys. Condens. Matter* 29 (2017) 465901.

[34] J. P. Perdew, K. Burke, M. Ernzerhof, Generalized gradient approximation made simple, *Phys. Rev. Lett.* 77 (1996) 3865–3868.

[35] S. Grimme, Semiempirical GGA-type density functional constructed with a long-range dispersion correction, *J. Comput. Chem.* 27 (2006) 1787–1799.

[36] M. Yamaguchi, T. Hashimoto, Magnetic Properties of Cr₃Te₄ in Ferromagnetic Region, *J. Phys. Soc. Jpn.* 32 (1972) 635–638.

[37] S. Ohta, Magnetic Properties of (Cr_{1-u}V_u)₃Te₄, *J. Phys. Soc. Jpn.* 54 (1985) 1076–1086.

[38] D. Babot, M. Wintenberger, B. Lambert-Andron, M. Chevreton, Propriétés magnétiques et conductibilité électrique des composés ternaires Cr₃Se_{4-x}Te_x, *J. Solid State Chem.* 8 (1973) 175–181.

[39] C. Chen, X. Chen, C. Wu, X. Wang, Y. Ping, X. Wei, X. Zhou, J. Lu, L. Zhu, J. Zhou, et al., Air-Stable 2D Cr₅Te₈ Nanosheets with Thickness-Tunable Ferromagnetism, *Adv. Mater.* 34 (2022) 2107512.

[40] C. Li, K. Liu, D. Jiang, C. Jin, T. Pei, T. Wen, B. Yue, Y. Wang, Diverse Thermal Expansion Behaviors in Ferromagnetic Cr_{1-δ}Te with NiAs-Type, Defective Structures, *Inorg. Chem.* 61 (2022) 14641.

[41] D. T. Wang, A. Göbel, J. Zegenhagen, M. Cardona, Raman scattering on α-Sn: Dependence on isotopic composition, *Phys. Rev. B* 56 (1997) 13167–13171.

[42] A. F. ANDRESEN, E. Zeppezauer, T. Boive, B. Nordström, C. Brändén, Magnetic structure of cr 2 te 3, cr 3 te 4, and cr 5 te 6, *Acta Chem. Scand.* 24 (1970) 3495–3509.

[43] W.-H. Jiao, Q. Tao, J.-K. Bao, Y.-L. Sun, C.-M. Feng, Z.-A. Xu, I. Nowik, I. Felner, G.-H. Cao, Anisotropic superconductivity in Eu(Fe_{0.75}Ru_{0.25})₂As₂ ferromagnetic superconductor, *EPL (Euro-physics Letters)* 95 (2011) 67007.

[44] M. Tinkham, *Introduction to Superconductivity*, Medtech, 2017.

[45] S. Ishida, D. Kagerbauer, S. Holleis, K. Iida, K. Munakata, A. Nakao, A. Iyo, H. Ogino, K. Kawashima, M. Eisterer, H. Eisaki, Superconductivity-driven ferromagnetism and spin manipulation using vortices in the magnetic superconductor EuRbFe₄As₄, *Proc. Natl. Acad. Sci.* 118 (2021) e2101101118.

[46] T. Hamasaki, T. Hashimoto, Y. Yamaguchi, H. Watanabe, Neutron diffraction study of Cr₂Te₃ single crystal, *Solid State Commun.* 16 (1975) 895–897.

[47] J. Dijkstra, C. F. van Bruggen, C. Haas, R. A. de Groot, Electronic band-structure calculations of some magnetic chromium compounds, *Journal of Physics: Condensed Matter* 1 (1989) 9163–9174.

[48] V. Ginzburg, Antagonie von magnetismus und supraleitung, *Journal of Experimental and Theoretical Physics* 4 (1957) 153.

[49] R. D. Parks, *Superconductivity*, Routledge, 2018. URL: <https://doi.org/10.1201%2F9780203737958>. doi:10.1201/9780203737958.

[50] J. S. Kim, R. K. Kremer, L. Boeri, F. S. Razavi, Specific Heat of the Ca-Intercalated Graphite Superconductor CaC₆, *Phys. Rev. Lett.* 96 (2006) 217002.

[51] Y. Liu, C. Petrovic, Critical behavior of the quasi-two-dimensional weak itinerant ferromagnet trigonal chromium telluride Cr_{0.62}Te, *Phys. Rev. B* 96 (2017) 134410.

[52] Y. Zhu, X. Kong, T. D. Rhone, H. Guo, Systematic search for two-dimensional ferromagnetic materials, *Phys. Rev. Materials* 2 (2018) 081001.

[53] S. Nakatsuji, N. Kiyohara, T. Higo, Large anomalous Hall effect in a non-collinear antiferromagnet at room temperature, *Nature* 527 (2015) 212–215.

[54] K. Kuroda, T. Tomita, M.-T. Suzuki, C. Bareille, A. Nugroho, P. Goswami, M. Ochi, M. Ikhlas, M. Nakayama, S. Akebi, R. Noguchi, R. Ishii, N. Inami, K. Ono, H. Kumigashira, A. Varykhalov, T. Muro, T. Koretsune, R. Arita, S. Shin, T. Kondo, S. Nakatsuji, Evidence for magnetic Weyl fermions in a correlated metal, *Nat. Mater.* 16 (2017) 1090–1095.

[55] N. Kanazawa, Y. Onose, T. Arima, D. Okuyama, K. Ohoyama, S. Wakimoto, K. Kakurai, S. Ishiwata, Y. Tokura, Large Topological Hall Effect in a Short-Period Helimagnet MnGe, *Phys. Rev. Lett.* 106 (2011) 156603.

[56] K. Shibata, X. Z. Yu, T. Hara, D. Morikawa, N. Kanazawa, K. Kimoto, S. Ishiwata, Y. Matsui, Y. Tokura, Towards control of the size and helicity of skyrmions in helimagnetic alloys by spin-orbit coupling, *Nat. Nanotechnol.* 8 (2013) 723.

[57] X. Yao, J. Chen, S. Dong, Controlling the helicity of magnetic skyrmions by electrical field in frustrated magnets, *New J. Phys.* 22 (2020) 083032.

[58] L. Zhou, J. Chen, X. Chen, B. Xi, Y. Qiu, J. Zhang, L. Wang, R. Zhang, B. Ye, P. Chen, X. Zhang, G. Guo, D. Yu, J.-W. Mei, F. Ye, G. Wang, H. He, Topological Hall Effect in Traditional Ferromagnet Embedded with Black-Phosphorus-Like Bismuth Nanosheets, *ACS Appl. Mater. Interfaces* 12 (2020) 25135–25142. PMID: 32338493.

[59] H. Li, L. Wang, J. Chen, T. Yu, L. Zhou, Y. Qiu, H. He, F. Ye, I. K. Sou, G. Wang, Molecular Beam Epitaxy Grown Cr₂Te₃ Thin Films with Tunable Curie Temperatures for Spintronic Devices, *ACS Appl. Nano Mater.* 2 (2019) 6809–6817.

- [60] X. Yu, Y. Onose, N. Kanazawa, J. H. Park, J. Han, Y. Matsui, N. Nagaosa, Y. Tokura, Real-space observation of a two-dimensional skyrmion crystal, *Nature* 465 (2010) 901–904.
- [61] W. Jiang, G. Chen, K. Liu, J. Zang, S. G. Te Velthuis, A. Hoffmann, Skyrmions in magnetic multilayers, *Physics Reports* 704 (2017) 1–49.
- [62] O. Meshcheriakova, S. Chadov, A. K. Nayak, U. K. Rößler, J. Kübler, G. André, A. A. Tsirlin, J. Kiss, S. Hausdorf, A. Kalache, W. Schnelle, M. Nicklas, C. Felser, Large Noncollinearity and Spin Reorientation in the Novel Mn₂RhSn Heusler Magnet, *Phys. Rev. Lett.* 113 (2014) 087203.
- [63] P. K. Rout, P. V. P. Madduri, S. K. Manna, A. K. Nayak, Field-induced topological Hall effect in the noncoplanar triangular antiferromagnetic geometry of Mn₃Sn, *Phys. Rev. B* 99 (2019) 094430.
- [64] B. Ding, Z. Li, G. Xu, H. Li, Z. Hou, E. Liu, X. Xi, F. Xu, Y. Yao, W. Wang, Observation of magnetic skyrmion bubbles in a van der Waals ferromagnet Fe₃GeTe₂, *Nano Letters* 20 (2019) 868–873.
- [65] D. A. Gilbert, B. B. Maranville, A. L. Balk, B. J. Kirby, P. Fischer, D. T. Pierce, J. Unguris, J. A. Borchers, K. Liu, Realization of ground-state artificial skyrmion lattices at room temperature, *Nat. Commun.* 6 (2015) 1–7.
- [66] M. Nakamura, D. Morikawa, X. Yu, F. Kagawa, T.-h. Arima, Y. Tokura, M. Kawasaki, Emergence of Topological Hall Effect in Half-Metallic Manganite Thin Films by Tuning Perpendicular Magnetic Anisotropy, *J. Phys. Soc. Jpn.* 87 (2018) 074704.
- [67] Y. Machida, S. Nakatsuji, Y. Maeno, T. Tayama, T. Sakakibara, S. Onoda, Unconventional anomalous hall effect enhanced by a noncoplanar spin texture in the frustrated kondo lattice Pr₂Ir₂O₇, *Phys. Rev. Lett.* 98 (2007) 057203.
- [68] Y. Taguchi, Y. Oohara, H. Yoshizawa, N. Nagaosa, Y. Tokura, Spin chirality, berry phase, and anomalous hall effect in a frustrated ferromagnet, *Science* 291 (2001) 2573–2576.
- [69] H. Wang, Y. Dai, G. M. Chow, J. Chen, Topological Hall transport: materials, mechanisms and potential applications, *Prog. Mater Sci.* (2022) 100971.
- [70] D. Feng, Z. Shen, Y. Xue, Z. Guan, R. Xiao, C. Song, Strain-induced magnetic phase transition, magnetic anisotropy switching and bilayer antiferromagnetic skyrmions in van der Waals magnet CrTe₂, *Nanoscale* 15 (2023) 1561.
- [71] Y. Wang, S. Kajihara, H. Matsuoka, B. K. Saika, K. Yamagami, Y. Takeda, H. Wadati, K. Ishizaka, Y. Iwasa, M. Nakano, Layer-Number-Independent Two-Dimensional Ferromagnetism in Cr₃Te₄, *Nano Lett.* 22 (2022) 9964–9971.
- [72] A. I. Liechtenstein, V. I. Anisimov, J. Zaanen, Density-functional theory and strong interactions: Orbital ordering in Mott-Hubbard insulators, *Phys. Rev. B* 52 (1995) R5467–R5470.
- [73] A. V. Chubukov, D. V. Efremov, I. Eremin, Magnetism, superconductivity, and pairing symmetry in iron-based superconductors, *Phys. Rev. B* 78 (2008) 134512.
- [74] I. I. Mazin, D. J. Singh, M. D. Johannes, M. H. Du, Unconventional Superconductivity with a Sign Reversal in the Order Parameter of LaFeAsO_{1-x}F_x, *Phys. Rev. Lett.* 101 (2008) 057003.
- [75] K. Terashima, Y. Sekiba, J. H. Bowen, K. Nakayama, T. Kawahara, T. Sato, P. Richard, Y.-M. Xu, L. J. Li, G. H. Cao, Z.-A. Xu, H. Ding, T. Takahashi, Fermi surface nesting induced strong pairing in iron-based superconductors, *Proc. Natl. Acad. Sci.* 106 (2009) 7330–7333.
- [76] J. Ruvalds, C. T. Rieck, S. Tewari, J. Thoma, A. Virosztek, Nesting mechanism for d-symmetry superconductors, *Phys. Rev. B* 51 (1995) 3797–3805.
- [77] T. Valla, A. V. Fedorov, J. Lee, J. C. Davis, G. D. Gu, The Ground State of the Pseudogap in Cuprate Superconductors, *Science* 314 (2006) 1914–1916.
- [78] S. Thirupathaiah, S. de Jong, R. Ovsyannikov, H. A. Dürr, A. Varykhalov, R. Follath, Y. Huang, R. Huisman, M. S. Golden, Y.-Z. Zhang, H. O. Jeschke, R. Valentí, A. Erb, A. Gloskovskii, J. Fink, Orbital character variation of the Fermi surface and doping dependent changes of the dimensionality in BaFe_{2-x}Co_xAs₂ from angle-resolved photoemission spectroscopy, *Phys. Rev. B* 81 (2010) 104512.

7. Supplementary Information

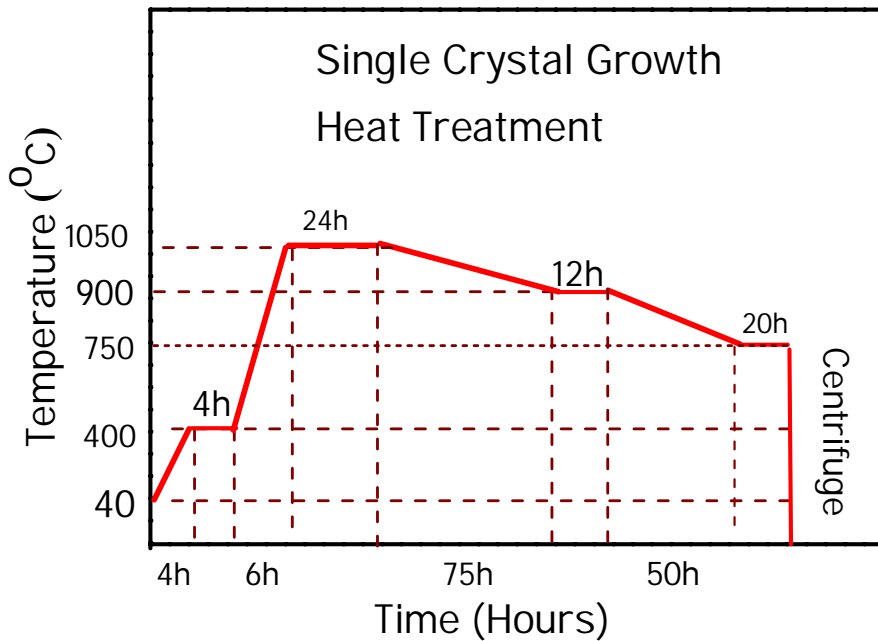


Figure 8: Heat treatment diagram of $\text{Sn}_{0.06}\text{Cr}_3\text{Te}_4$ single crystal growth.

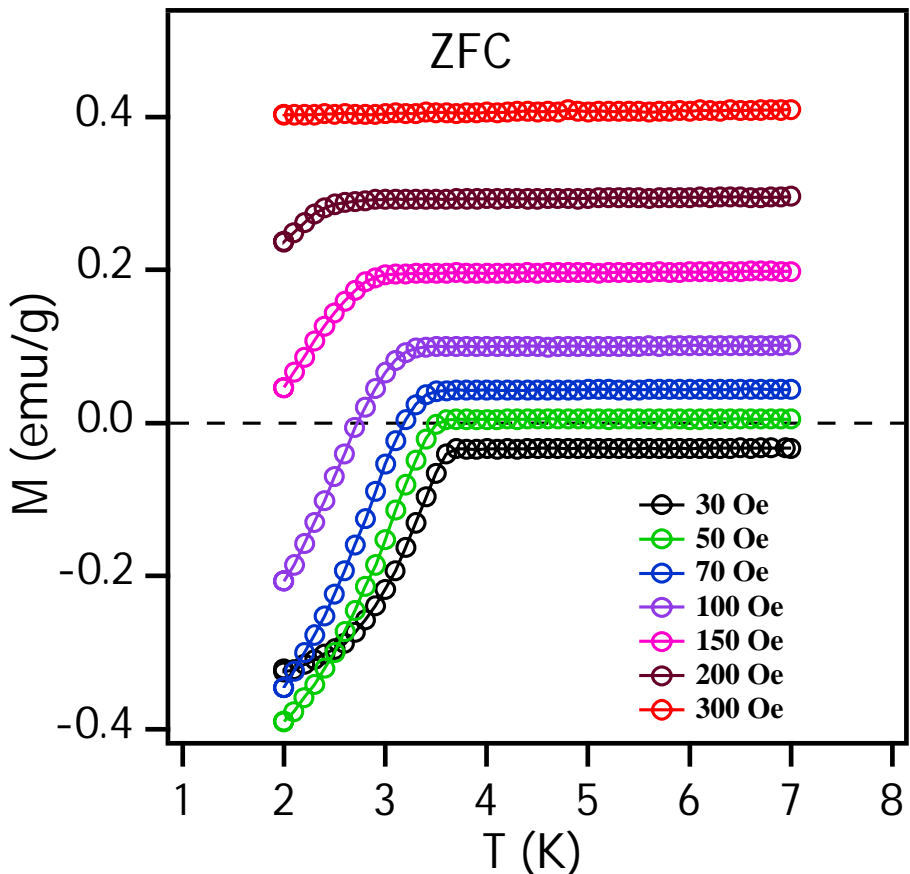


Figure 9: (a) Magnetization plotted as a function of temperature measured at various magnetic fields for $H \parallel a$ from $\text{Sn}_{0.06}\text{Cr}_3\text{Te}_4$. Clear Meissner effect with negative magnetization has been noticed below T_c for the fields up to 100 Oe. Beyond 150 Oe, though a magnetization drop is noticed below T_c , Meissner effect is absent. At 300 Oe, no drop in magnetization is noticed.

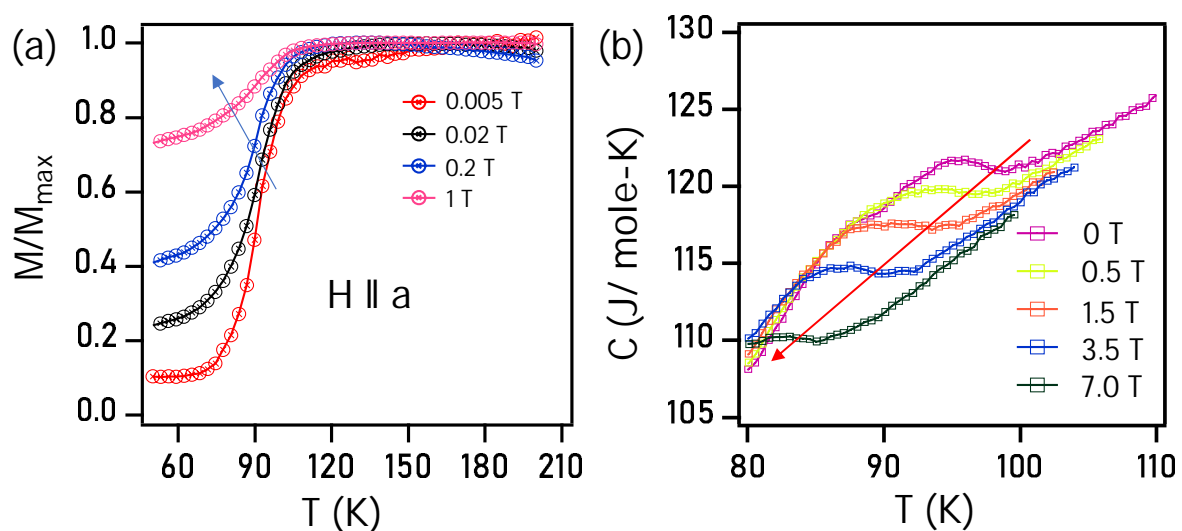


Figure 10: (a) Magnetization and (b) Specific heat plotted as a function of temperature, measured under various magnetic fields with $H \parallel a$ for $\text{Sn}_{0.06}\text{Cr}_3\text{Te}_4$. Both magnetization and specific heat data suggest that the magnetic transition found at 98 K is of the canted AFM-type as the magnetic transition temperature decreases with increasing the field.

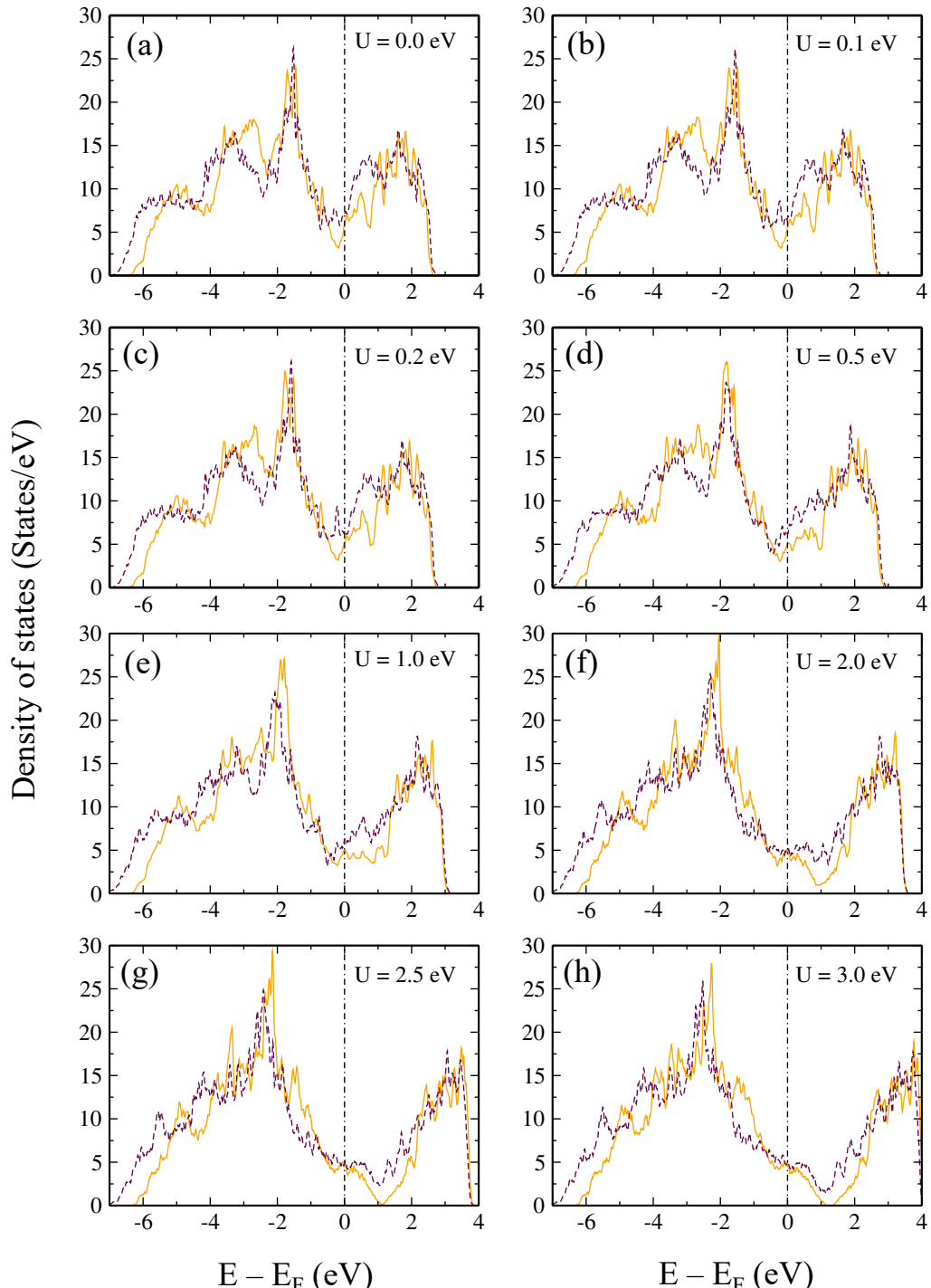


Figure 11: Density of states of parent Cr_3Te_4 (yellow solid line) and 6% Sn intercalated Cr_3Te_4 (maroon dashed line) calculated at different values of the Hubbard (U) parameter.

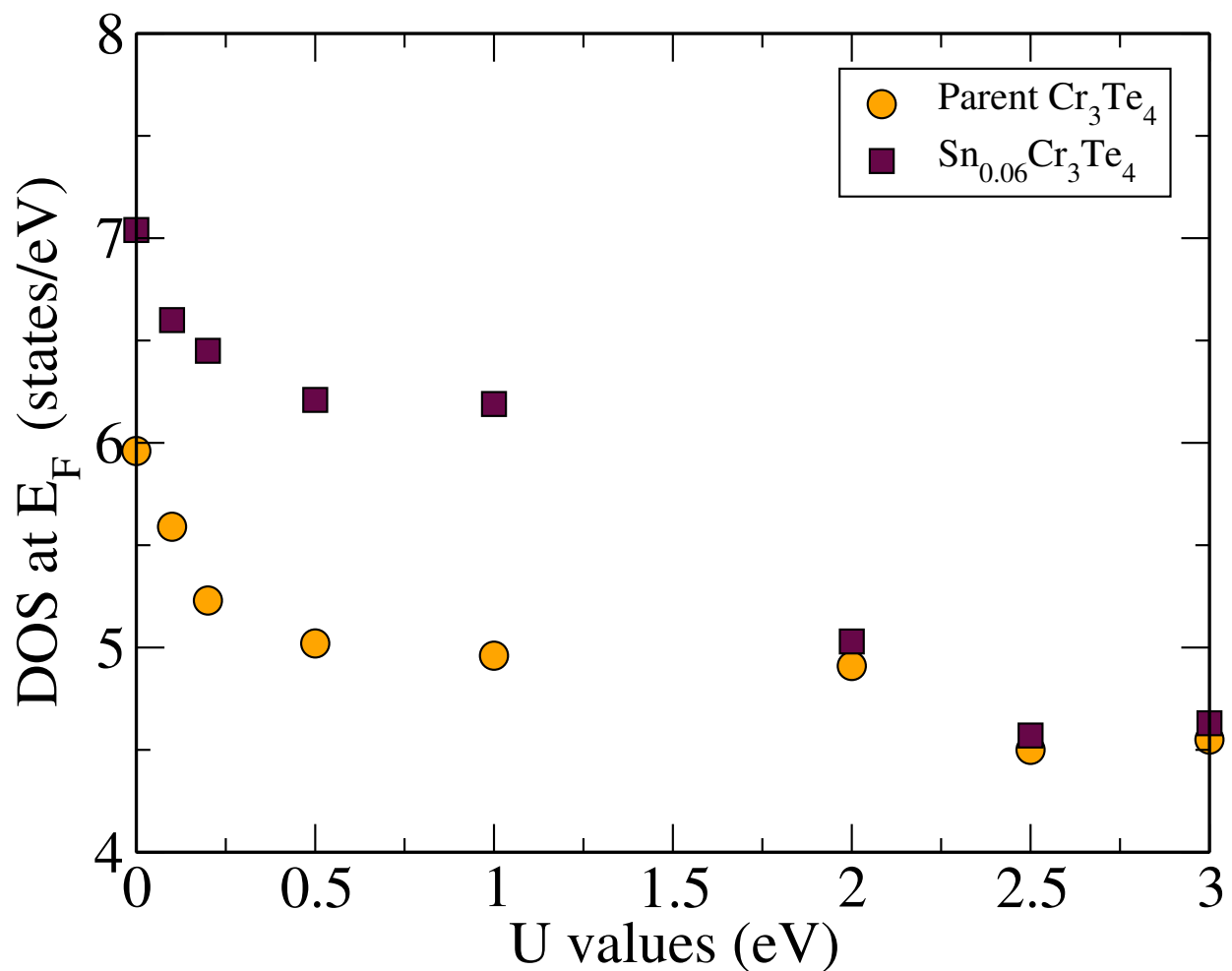


Figure 12: DOS at E_F as a function of U . Yellow circles and maroon squares represent the parent Cr_3Te_4 and $\text{Sn}_{0.06}\text{Cr}_3\text{Te}_4$ systems, respectively.

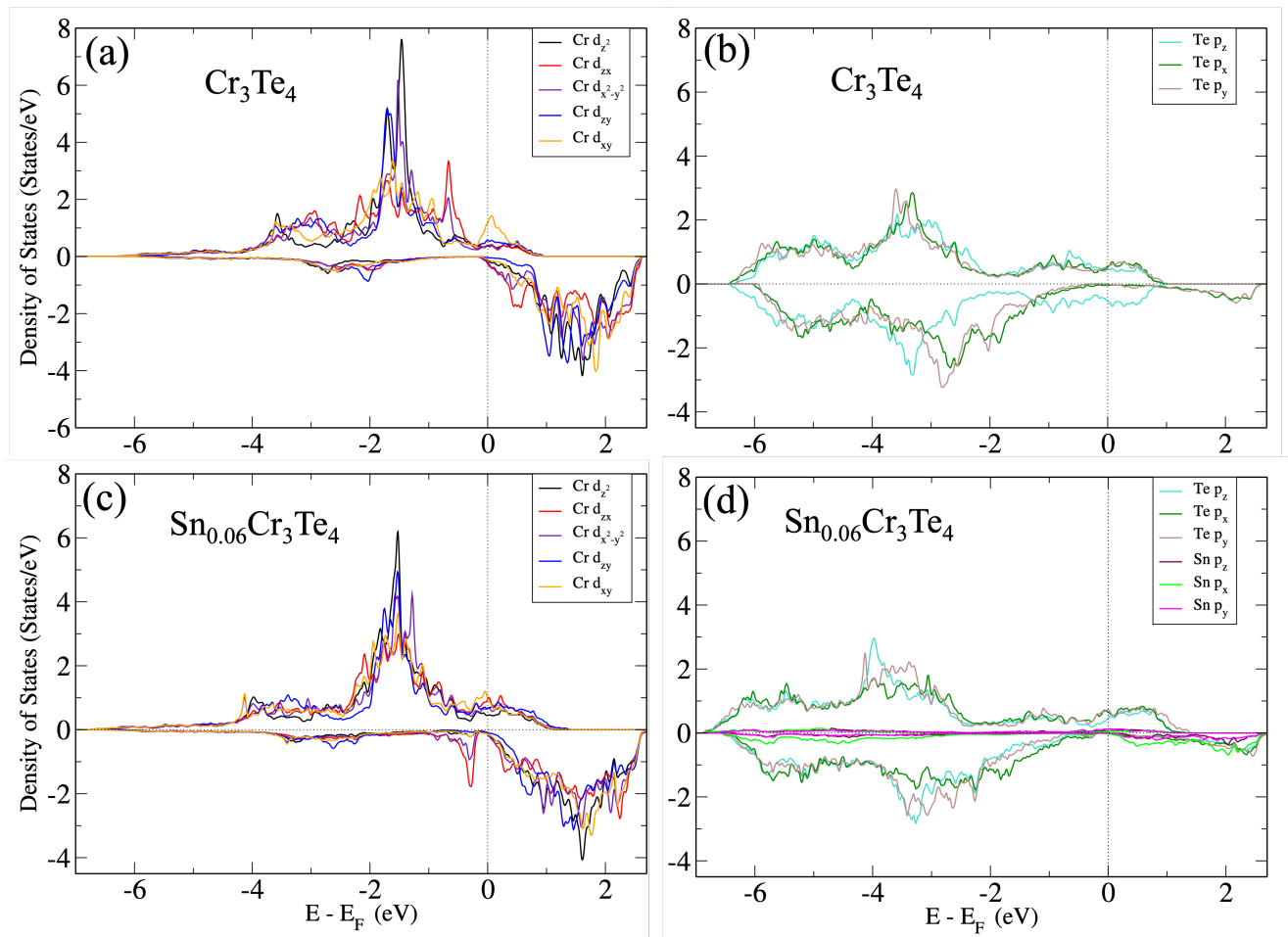


Figure 13: Projected density of states (PDOS) from parent Cr_3Te_4 for Cr-*d* orbitals (a) and Te-*p* orbitals (b). PDOS of Sn intercalated system for Cr-*d* orbitals (c), and for *p* orbitals of Te and Sn atoms (d). The negative values indicate down-spin states, while the positive values show the up-spin states.